Title

Time-series analysis of surface deformation at Brady Hot Springs geothermal field (Nevada) using interferometric synthetic aperture radar

Authors

Ali, ST
Akerley, J
Baluyut, EC
et al.

Publication Date

2016-05-01

DOI

10.1016/j.geothermics.2016.01.008

Peer reviewed

Geothermics
Volume 61, May 2016, Pages 114-120

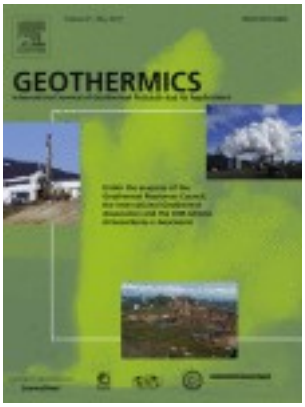

Time-series analysis of surface deformation at Brady Hot Springs geothermal field (Nevada) using interferometric synthetic aperture radar

Author links open overlay panelS.T.Ali[a]J.Akerley[b]E.C.Baluyut[a]M.Cardiff[a]N.C.Davatzes[c]K.L.Feigl[a]W.Foxall[d]D.Fratta[a]R.J.Mellors[e]P.Spielman[b]H.F.Wang[a]E.Zemach[b]
Show more

https://doi.org/10.1016/j.geothermics.2016.01.008Get rights and content

Abstract

We analyze interferometric synthetic aperture radar (InSAR) data acquired between 2004 and 2014, by the ERS-2, Envisat, ALOS and TerraSAR-X/TanDEM-X satellite missions to measure and characterize time-dependent deformation at the Brady Hot Springs geothermal field in western Nevada due to extraction of fluids. The long axis of the ~4 km by ~1.5 km elliptical subsiding area coincides with the strike of the dominant normal fault system at Brady. Within this bowl of subsidence, the interference pattern shows several smaller features with length scales of the order of ~1 km. This signature occurs consistently in all of the well-correlated interferometric pairs spanning several months. Results from inverse modeling suggest that the deformation is a result of volumetric contraction in shallow units, no deeper than 600 m, likely associated with damaged regions where fault segments mechanically interact. Such damaged zones are expected to extend downward along steeply dipping fault planes, providing a high permeability conduit to the production wells. Using time series analysis, we test the hypothesis that geothermal production drives the observed deformation. We find a good correlation between the observed deformation rate and the rate of production in the shallow wells. We also explore mechanisms that could potentially cause the observed deformation, including thermal contraction of rock, decline in pore pressure and dissolution of minerals over time.

- **Previous** article
- **Next** article

Keyword

InSAR deformation

1. Introduction

The Brady Hot Springs geothermal field is located approximately 80 km east-northeast of Reno, in the Hot Spring Mountains of northwestern Nevada. The area surrounding the field is dominated by a network of north-northeast trending, steeply dipping, en echelon normal faults, as mapped by Faulds et al. (2003) and shown in Fig. 1. A ~15 megawatt geothermal plant at Brady has been generating power since 1992. Six production wells, located near a prominent bend in the normal fault system (Fig. 1) are used to withdraw hot water from depths of 400 to 1850 m. Following generation of electricity, most of the spent brine is recycled back into the subsurface, between depths of 200 and 300 m, via two injection wells located 1500–2500 m away in the north-northeast direction, along the strike of the predominant fault system, whereas the rest is

diverted away from the field. The geothermal reservoir is hosted in layered Tertiary volcanic rocks, including welded tuff, rhyolite and meta-sediments overlying Mesozoic crystalline intrusions (Jolie et al., 2012, Siler and Faulds, 2013). The primary production interval reaches temperatures of ~175 °C at depths of 1000–2000 m (Benoit and Butler, 1983, Shevenell et al., 2012). The net extraction rate, averaged over the 2004–2014 time interval, is ~0.2 m^3/s.

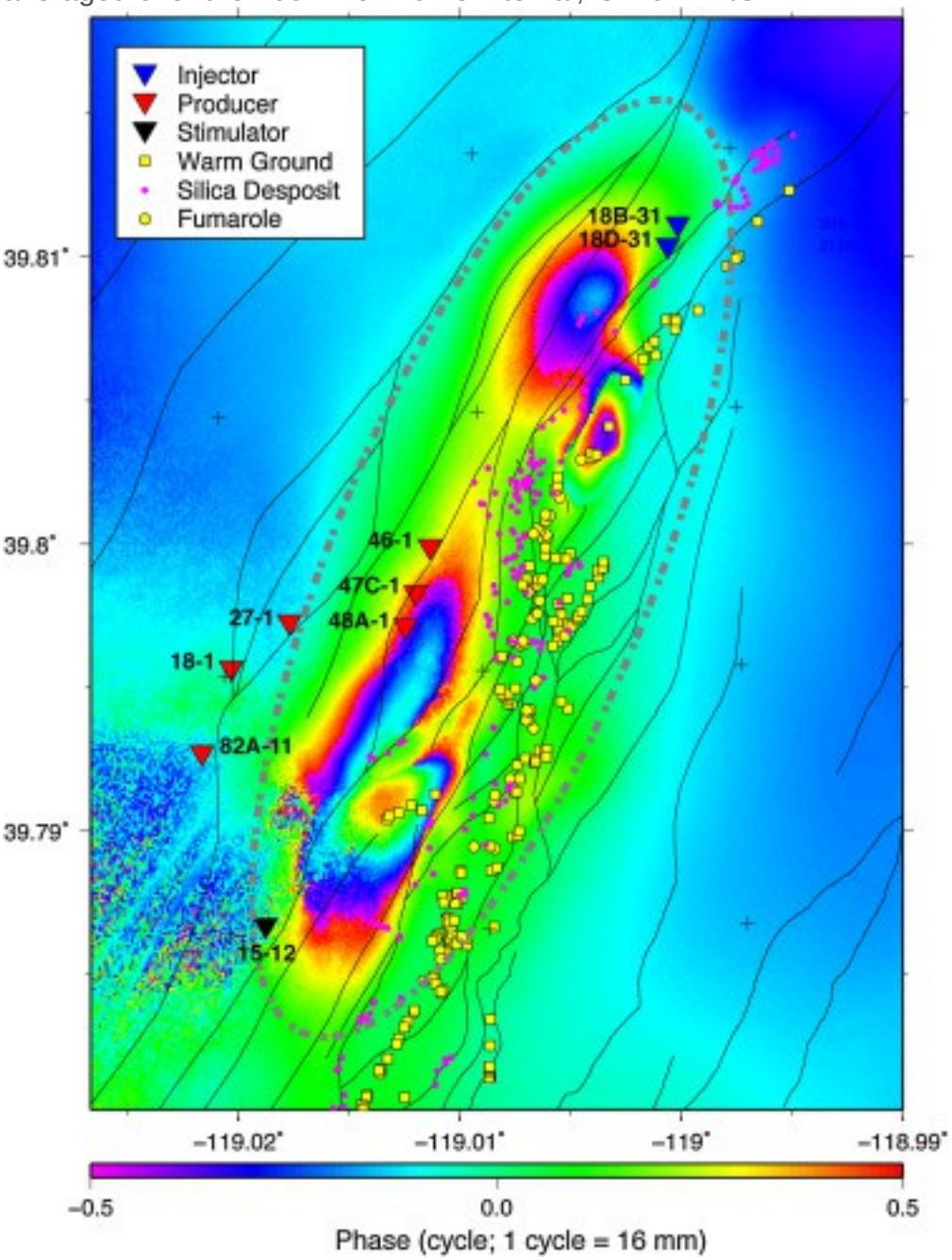

1. Download high-res image (1MB)
2. Download full-size image

Fig. 1. Map showing location of the Brady Hot Springs geothermal field. The fault map is from Faulds et al. (2010) and surface hydrothermal activity is from Coolbaugh et al. (2004). Injection wells are shown by blue triangles and producing wells are shown by red triangles. Fiducial crosses indicate 1000-meter grid in easting and northing of the Universal Transverse Mercator (UTM) projection (Zone 11). The TSX interferogram in the background shows wrapped phase change values over the 308-day interval from December 24, 2011 to October 27, 2012. One colored fringe corresponds to one cycle of phase change, or 16 mm of range change. The dotted and dashed grey line delimits the broad deforming zone described in Section 2.1. (For interpretation of the references to color in this figure legend, the reader is referred to the web version of this article.)

Withdrawal of fluids from the subsurface can cause deformation through a number of processes, including thermal contraction of rock, change in pore pressure, and dissolution/alteration of minerals. At the surface, this deformation can be measured using interferometric synthetic aperture radar (InSAR). InSAR uses the phase difference between two SAR images, acquired at two different points in time (epochs), to create an interferogram (e.g., Massonnet and Feigl, 1998). The resulting map of ambiguous wrapped phase contains information about ground deformation, topography, and atmospheric changes. After correcting the interferogram for topography, an unwrapping algorithm is used to estimate the range change along the line of sight. By analyzing the pattern of deformation, we can gain insight into the underlying geomechanical processes and the plumbing of the reservoir which can aid the operator to better manage the geothermal resource. This approach has been used to study deformation at several geothermal fields, including, Cerro Prieto, Mexico (Carnec and Fabriol, 1999, Sarychikhina et al., 2007), Coso, California (Fialko and Simons, 2000, Wicks et al., 2001), Dixie Valley, Nevada (Foxall and Vasco, 2003), Brady, Nevada (Oppliger et al., 2004, Oppliger et al., 2006, Shevenell et al., 2012), Taupo Volcanic Zone, New Zealand (Chang et al., 2005, Hole et al., 2007), Svartsengi, Iceland (Jonsson, 2009, Masters, 2011), Imperial Valley, California (Eneva et al., 2009, Eneva et al., 2012), San Emidio, Nevada (Eneva et al., 2011) and The Geysers, California (Vasco et al., 2013). Most of these studies show rates of deformation that remain fairly constant over time scales of years. At Brady, Oppliger et al., 2004, Oppliger et al., 2006 applied InSAR to map deformation resulting from geothermal production between 1997 and 2002, using images acquired by the C-band radar aboard the ERS satellite of the European Space Agency (ESA), and interpreted the cm-scale signal in terms of a contracting aquifer. In this study, we use multiple images acquired between 2004 and 2014 by several satellite missions, including ERS-2, Envisat, ALOS, TerraSAR-X (TSX)

and TanDEM-X (TDX), to measure and characterize the time-dependent deformation at Brady.

2. Data and methods

2.1. SAR interferometry

We analyze 139 SAR images acquired by the ERS-2, Envisat (McLeod et al., 1998), ALOS (Igarashi, 2001), TSX (Pitz and Miller, 2010) and TDX (Krieger et al., 2007) satellite missions between 2004 and 2014 and combine them to form 354 distinct interferometric pairs (Table S1). To generate interferograms from ERS-2, Envisat, and ALOS data, we use GMTSAR, an open-source code developed by Sandwell et al. (2011). For the TSX and TDX data, we generate interferograms using the DIAPASON software developed by the French Space Agency CNES (Massonnet and Rabaute, 1993, Massonnet and Feigl, 1998). The topographic contribution to the interferograms created in DIAPASON is removed using a digital elevation model (DEM) with 10 m posting from the National Elevation Dataset (Gesch et al., 2002). For interferograms processed with GMTSAR, we use a DEM with 1 arc-second posting from the Shuttle Radar Topographic Mission (Farr et al., 2007).
For example, the observed wrapped phase change values for the TSX pair spanning a 308-day time interval between December 24, 2011 and October 27, 2012 are shown in Fig. 1. One fringe of phase change in this interferogram corresponds to 16 mm of range change along the radar line of sight between the satellite and the ground. The wrapped phase values have been filtered using their two dimensional spectra (Goldstein and Werner, 1998). The spatial pattern of the deformation is aligned parallel to the north-northeast strike of predominant fault system, including the 4-km-long Brady normal fault, and the trend of the associated fumaroles. The interferogram shows several signatures of varying dimension. For example, a broad, elliptically shaped area roughly 4 km long by 1.5 km wide (outlined by the dotted and dashed grey line), that is consistent with earlier observations (Oppliger et al., 2004, Oppliger et al., 2006). Within this broad bowl, we observe several smaller elliptical features, with length scales ranging from 1 to 2 km. The major axes of each of these subsidence bowls trend NNE, following the bending trace of the normal fault strands (black lines in Fig. 1). The smaller bowls are centered along strike, but more than 0.5 km away from the two injection wells in the northeast part of the field. Similarly, the larger bowl is centered approximately ~1 km along strike from the producing wells in the southwest part of the field. These signatures are consistently observed in all interferograms spanning more than a year (Fig. S1). Pairs spanning less than year show only the short scale features that abut the

producing and injection wells. Using pairwise logic (Massonnet and Feigl, 1995), we reject the possibility that the observed signatures are due to imprecise orbital trajectories or atmospheric perturbations.

2.2. Inverse modeling

To gain insight into the sources causing the deformation observed in the interferograms, we perform non-linear inverse modeling using unwrapped range change rate as the observable quantity. To unwrap the phase values, we use the statistical-cost, network-flow phase-unwrapping algorithm developed by Chen and Zebker (2001). Following unwrapping, we account for any unmodeled effects in the satellite orbits by estimating three parameters describing a planar ramp and subtracting it from the range values across the entire scene. Finally, we calculate the range change rate in millimeters per year.

To describe the signatures in the interferograms, we use an elastic model where observed deformation is attributed to change in volume at depth. We model the reservoirs using a combination of mode-I, tensile dislocations in rectangular prisms, embedded in a halfspace with uniform elastic material properties (Okada, 1985). The tensile dislocating sources are especially appropriate because the thickness of an aquifer or reservoir is usually smaller than its length or width. By estimating the parameters in this idealized model, we can gain insight into the geometry and location of the reservoir, e.g., its extent and depth. The estimated volume change in the model that fits the surface deformation is presumably due to injection and/or extraction of fluids, as discussed above. To solve the inverse problem, we use an iterative, gradient based inversion scheme that uses a Taylor series to approximate the fitting function (Ali and Feigl, 2012). The inversion procedure minimizes the L1 norm of the residual between the observed and modeled values of the range change, averaged over all points in the dataset. Uncertainties are calculated using the bootstrapping procedure (Efron and Tibshirani, 1986) described in Ali et al. (2014).

Since the rate of hot fluid withdrawal exceeds the rate of injection, the resulting total is net extraction that decreases the volume of the reservoir. Our mechanical model includes four tensile dislocating sources. The free parameters for each source include position, geometry (i.e., length, width, dip, and strike) and the opening, which is positive for an expanding source and negative for a contracting source. In addition, we estimate a nuisance parameter that accounts for systematic offsets in range change rate as an additive constant. First, we perform inversion using the stack (average) of all the maps of range change rate, in each track, in order to estimate the geometrical parameters.

This procedure improves the signal-to-noise ratio as random noise will average to zero. For example, Fig. 2shows the stacked range change rate, in mm/year, averaged for all successful TSX/TDX pairs in Track 53, the modeled range change calculated using the final estimate of parameters, following the inversion, and the residual difference between the stacked and the modeled rates of range change. During inversion, the cost, defined as the L1 misfit of the range change rate, averaged over all pixels, decreases to less than 1 mm/year. The main features, such as the elliptical lobes near production wells in the south, and near the injection wells, are reproduced by the model. The estimated parameters are listed in Table 1 along with their bootstrap uncertainties. In the second step, we fix the geometry of all four sources and perform inversion for each individual pair in the track to estimate the opening parameter for each individual source, along with the nuisance parameter. For example, Fig. 3 shows the results for a single pair in Track 53, spanning the 363-day interval from May 13, 2013 to May 11, 2014. For this pair the final cost is 2.2 mm.

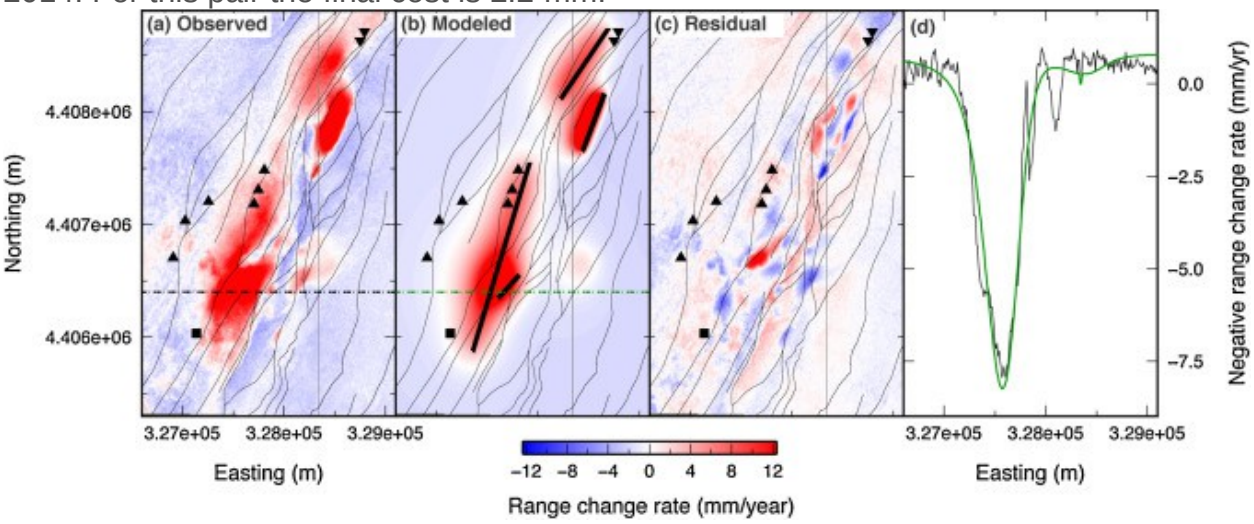

1. Download high-res image (886KB)
2. Download full-size image

Fig. 2. (a) Average rate of range change, in mm/year, calculated from 90 unwrapped TSX/TDX interferometric pairs in Track 53 spanning 2011–2015. Coordinates are northing and easting in kilometers in zone 11 of the Universal Transverse Mercator projection using the WGS84 ellipsoid. (b) Modeled unwrapped range change rate, in mm/year, calculated from the final estimate of the parameters. (c) Residual values of the range change calculated by subtracting the modeled values from the observed values. Thin solid lines represent the surface trace of faults, triangles represent producers, inverted triangles represent injection wells and square represents the location of well 15-12. Thick solid lines in (b) represent the surface projections of the modeled sources.

(d) Observed and modeled rate of range change, across a cross-section shown by dashed lines in (a) and (b), respectively.

Table 1. Parameters estimated for the elastic model consisting of four, mode-I, rectangular tensile dislocations in elastic half-space (Okada, 1985), using the averaged/stacked rate of range change in Track 53 (TSX/TDX) shown in Fig. 2.

Parameter	Estimated value	Uncertainty
Okada1 length (m)	1729.606	119.439
Okada1 width (m)	5.007	0.275628
Okada1 depth (m)	277.686	36.1025
Okada1 dip (deg)	6.412	4.66619
Okada1 strike (deg)	18.520	2.43446
Okada1 east (m)	327,638.515	21.28
Okada1 north (m)	4,406,713.126	48
Okada1 opening (m)	−0.952	0.107816
Okada2 length (m)	738.462	111.717
Okada2 width (m)	5.036	0.409102
Okada2 depth (m)	221.930	54.8961
Okada2 dip (deg)	−9.459	8.56973
Okada2 strike (deg)	36.797	6.41109
Okada2 east (m)	328,458.785	31.875
Okada2 north (m)	4,408,425.726	32.5
Okada2 opening (m)	−0.818	0.166806
Okada3 length (m)	516.322	37.2377
Okada3 width (m)	5.007	0.28433
Okada3 depth (m)	100.998	13.9591
Okada3 dip (deg)	−34.252	10.6134
Okada3 strike (deg)	22.992	3.39852
Okada3 east (m)	328,547.951	13.8
Okada3 north (m)	4,407,906.391	16.5
Okada3 opening (m)	−1.173	0.152854
Okada4 length (m)	255.253	40.7995
Okada4 width (m)	5.845	0.62326
Okada4 depth (m)	273.394	35.5125
Okada4 dip (deg)	−26.515	13.6735

Parameter	Estimated value	Uncertainty
Okada4 strike (deg)	44.716	17.1364
Okada4 east (m)	327,713.976	36.565
Okada4 north (m)	4,406,448.995	43.25
Okada4 opening (m)	−2.483	0.233498
Rate of total volume increase (m^3/yr)	−18887.7	168.5

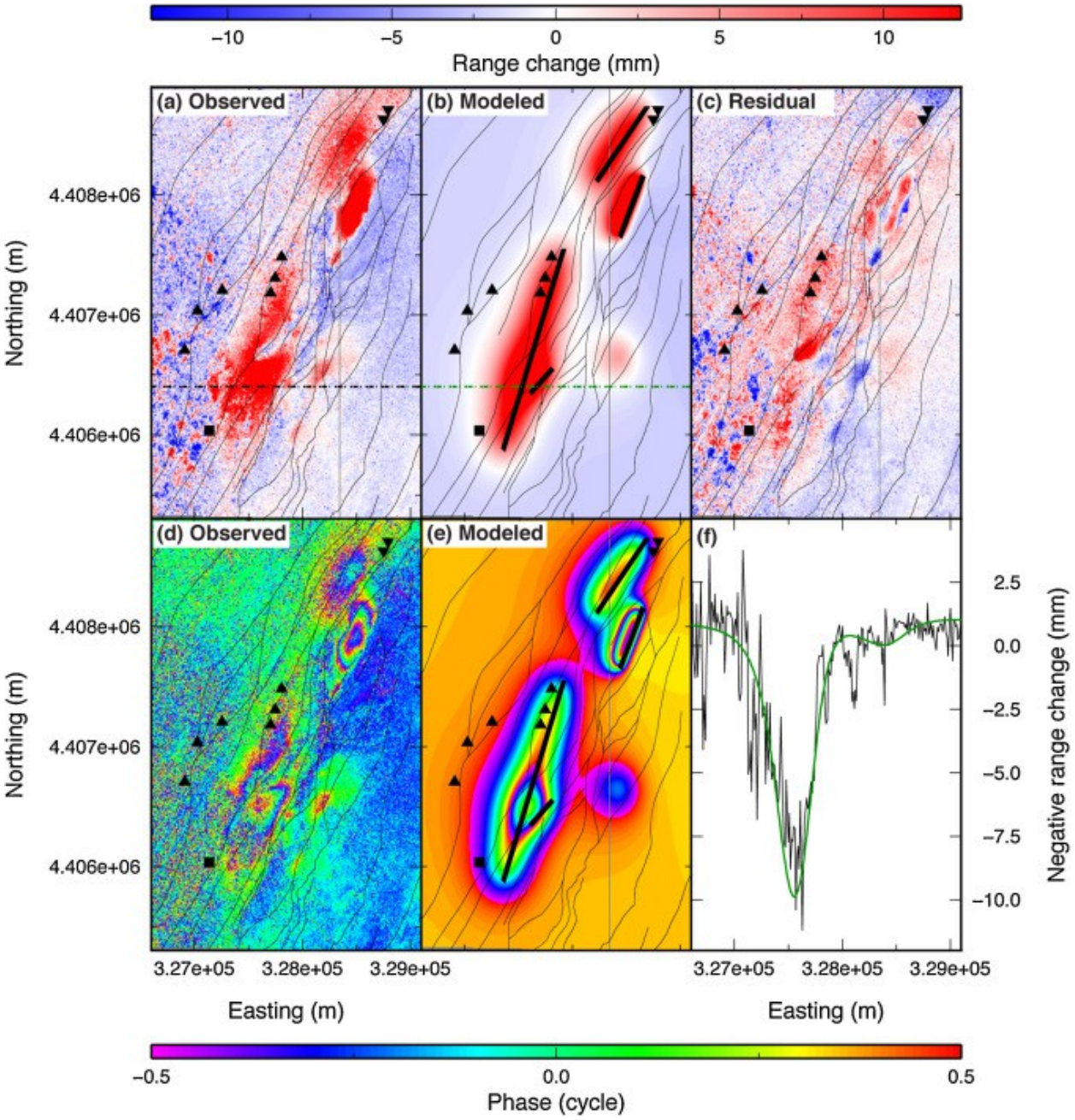

1. Download high-res image (3MB)
2. Download full-size image

Fig. 3. (a) Range change, in mm, calculated by unwrapping phase values from a TSX interferometric pair, spanning the 363-day interval from May 13, 2013 to May 11, 2014, shown in (d). Coordinates are northing and easting in kilometers in zone 11 of the Universal Transverse Mercator projection using the WGS84 ellipsoid. (b) Modeled range change, in mm, calculated from the final estimate of the parameters. (c) Residual values of the range change calculated by subtracting the modeled values from the observed values. (e) Modeled wrapped phase, calculated from the final estimate of the parameters. (f) Observed and modeled range change, across a cross-section shown by dashed lines in (a) and (b), respectively. One colored fringe in (d) and (e) corresponds to one cycle of phase change, or 16 mm of range change.

The estimated depths of the sources range from ~100 m for the shallowest deforming source near the injection wells to ~300 m for source near producing wells that results in the long wavelength signal. The estimates of tensile closing rates for the sources are between 1.0 and 2.5 m/year. As shown in Fig. 2, the strikes of the sources coincide with the strike of the predominant fault system. This result, along with small (but significant) estimates for width (~5 m), suggests that the deforming sources are associated with the faults.

We repeat the above procedure(s) for 354 interferometric pairs across 8 separate tracks to estimate model parameters. The geometry of various sources, e.g., their estimated length, width and strike, does not vary substantially across different tracks. Their estimated depth, however, ranges from ~100 m for the shallowest source to ~600 m for the deepest source. We then combine the estimated length, width and opening of corresponding sources to calculate the total rate of volume change for the time interval spanned by each pair. This calculation provides a scalar quantity that is convenient for studying the temporal evolution of the deformation. The estimated rate of volume change, in m^3/year, for each pair is shown in Fig. 4. The average value is $48.2 \pm 0.1 \times 10^3$ m^3/year or about 1.5 liter/s. However, the rate is not constant in time and appears to be decreasing, almost linearly since 2004, at least over the long term. Over shorter time scales, e.g., between 2012 and 2014, the variations do not show a clear non-linear pattern.

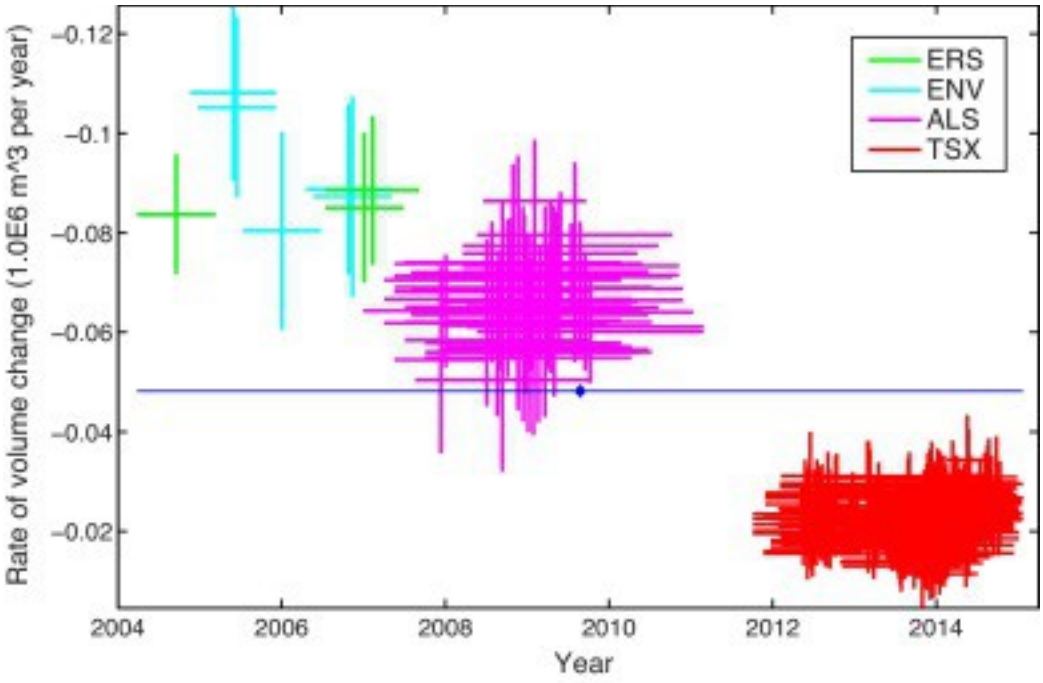

1. Download high-res image (170KB)
2. Download full-size image

Fig. 4. Cumulative rate of volume change calculated from the final estimate of parameters, for each pair, along with uncertainties (vertical bars) which have been scaled by the square root of the mean squared error from the temporal adjustment. Horizontal bars indicate time span for each interferometric pair.

2.3. Time-series analysis

In order to evaluate the time dependence, we perform time-series analysis using temporal adjustment. This procedure converts the rate of volume change estimated over individual interferometric pairs spanning different time intervals into the integrated volume at each point in time (e.g., Schmidt and Bürgmann, 2003, Beauducel et al., 2000, Feigl and Thurber, 2009, Feigl et al., 2014). To do so, we use the GraphTreeTA method of temporal adjustment (Baluyut et al., 2015unpublished manuscript) Because the rate of volume change is not constant (Fig. 4), we assume a piecewise linear parameterization for the temporal function that includes 8 segments, each spanning between 1 and 2 years. The volumetric rates of change estimated from the 354 pairs are weighted by the inverse of their covariance. The off-diagonal elements of this data covariance matrix account for the temporal correlation between interferometric pairs sharing a common epoch (e.g., Biggs et al., 2007). Each of the 8 free parameters in the model for the time dependence corresponds to the rate of change during the corresponding time interval. These 8 parameters are estimated, along with their

uncertainties, using standard weighted least squares (e.g., Aster et al., 2011). The 1-sigma uncertainties have been scaled by the weighted root mean squared scatter of the residuals. The number of free parameters in the temporal adjustment represents a trade-off between fitting the data and smoothing the model. Using a polynomial parameterization of order two yields a mean squared error value of 0.42, which is significantly worse than 0.26 found using a piecewise linear parameterization, respectively, by an *F*-test with 95% confidence. The results of temporal adjustment are shown in Fig. 5 (and Fig. S2) along with their uncertainties. The trend of the curve (solid black line) suggests that the underlying processes are continuous in time.

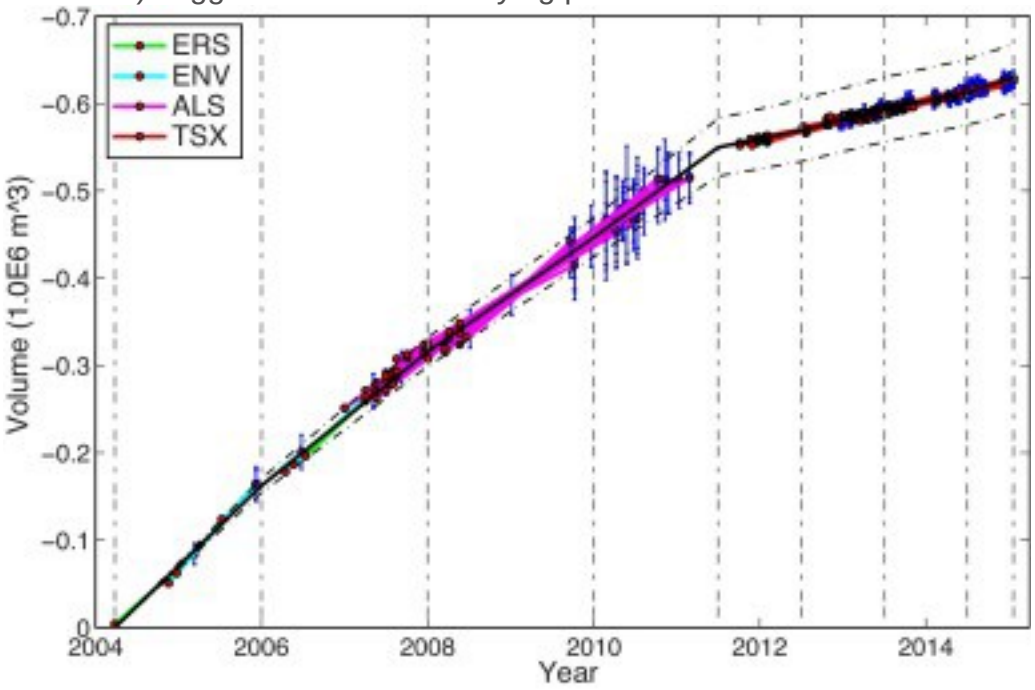

1. Download high-res image (170KB)
2. Download full-size image

Fig. 5. Volume change as a function of time as estimated from the individual pairs using temporal adjustment, assuming a piecewise linear model. Each colored line segment represents an individual InSAR pair connecting the first epoch with the second epoch. The mid-point of each time interval is taken as a reference and plotted arbitrarily on the modeled curve (black). The slope of each colored line segment denotes the rate of volume change estimated from the corresponding InSAR pair. A blue bar, drawn at the second epoch for each pair, denotes the uncertainty. (For interpretation of the references to color in this figure legend, the reader is referred to the web version of this article.)

To gain more insight into the processes, we compare the InSAR derived time series to the flow rates in various producing wells that were active between 2004 and 2014, along

with the time series estimated from InSAR. While these are two different quantities, i.e., the measured volume of water extracted versus decrease in the modeled volume of the reservoir, it can tell us if the deformation is being preferentially caused by certain wells or a group of wells. We do the comparison by calculating the correlation coefficient R between the two quantities.

We find good correlation between the volume change estimated from InSAR analysis and the production in shallow wells. Specifically, the strongest correlations occur in three cases, i.e., (i) wells 48A-1, 47C-1 and 46-1 summed together (R = 0.9954), (ii) well 48A-1 (R = 0.9936), and (iii) well 47C-1 (R = 0.9830). In each of these three cases, we find that the rate of production decreases with time, as does the rate of volumetric decrease as estimated from InSAR data. On the other hand, we find that the rate of production in deeper wells, i.e., wells 82A-11, 27-1 and 18-1, both individually and together, increases over time. This mismatch is reflected in the relatively low values ($R \leq 0.9548$) of the correlation coefficient. This result suggests that that the deformation is likely being caused by wells 48A-1, 46-1 and 47C-1, given their close proximity.

3. Discussion

Subsidence due to geothermal production can be caused by a number of processes, including: (i) gradual thermal cooling of reservoir, especially near injection wells, that recycle the cooler brine back into the subsurface, (ii) sediment compaction due to decreasing pore pressure and desaturation, and (iii) dissolution and transport of minerals in the flowing brine.

The temperature of produced fluids at geothermal fields decreases slowly over time. Subsidence, however, depends on the volume of rock that is cooled. If we assume that the thermal energy gained by the water equals the energy lost by the rock, we have,

$$(1) c_{prod}\rho_{prod}V_{prod}T_{prod} - c_{inj}\rho_{inj}V_{inj}T_{inj} = c_{rock}\rho_{rock}\Delta T_{rock}V_{rock},$$

where c is the specific heat capacity, ρ is the density, V is the volume, and T is the temperature. Subscripts *prod*, *inj*, and *rock* represent values for produced water, injected water and reservoir rock, respectively. Because liquid water at Brady does not flash to steam, we neglect the latent heat of vaporization. Since the volume of the rock cooled is the same as the volume of rock that contracts,

$$(2) \Delta V_{rock} = \alpha_{rock}\Delta T_{rock}V_{rock},$$

where α is the coefficient of thermal expansion. Substituting, we find

$$(3) \Delta V_{rock} = \alpha_{rock}c_{prod}\rho_{prod}V_{prod}T_{prod} - c_{inj}\rho_{inj}V_{inj}T_{inj}\rho_{rock}c_{rock}.$$

Assuming ρ_{prod} = 902 kg/m^3, ρ_{inj} = 972 kg/m^3, c_{prod} = 4360 J/kg/K, c_{inj} = 4198 J/kg/K, ρ_{rock} = 2 750 kg/m^3, c_{rock} = 800 J/kg/K, α_{rock} = 10^{-5} K^{-1}, V_{prod} = 0.5607 m^3 (per second), T_{prod} = 420 K

(average value for producers), V_{inj} = 0.3318 m^3 (per second), and T_{inj} = 355 K (average value for injection wells), we obtain ΔV_{rock} = 2.0 liters (per second). This value is ~ 1.5 times the average rate of volume change over 2004–2014 estimated from the modeling of InSAR data (Fig. 4). If the assumptions in this simple model are correct then we infer that shallow contracting sources, which presumably have a higher fracture density and therefore can cool faster than the rest of the reservoir, provide more than half of the energy. Any contraction in the larger, deeper reservoir, tapped by wells 82A-11, 27-1, and 18-1, is likely to result in a subsidence signature that is too broad to be observed in the InSAR pairs spanning less than 2 years.

Another possible explanation for the observed deformation involves compacting sediments in multiple, laterally separated zones, likely associated with faults. Such zones, potentially comprising anomalously soft, highly porous compressible sediments (e.g., expansive clays), could deform due to decrease in pore pressure, following steady decline in the water table, as fluids are extracted for geothermal production. Declining pore pressure has been suggested as a plausible mechanism for subsidence at a number of geothermal fields, e.g., those in the Taupo Volcanic Zone in New Zealand (Allis and Zhan, 2000, Bromley et al., 2009). At Brady, precise measurements of water levels near the production wells over the 2004–2014 interval are not available. Because the depth of the shallowest producing well is ~400 m, the maximum drop in water level that is theoretically possible, following the start of production in 1992, is 400 m or ~18 m per year. If this indeed is the case, then the compaction due to the concomitant increase in effective stress can be estimated from the 1-dimensional settlement equation (Terzaghi and Peck, 1968):

(4)$\delta c = \frac{Cc}{1+e0} H \log \frac{\sigma zf'}{\sigma z0'}$

where δ_c is the displacement by settlement, C_c is the compression index, e_0 is the initial void ratio, H is the thickness of the compacting layer, and $\sigma zf'$ and $\sigma z0'$ are the final and initial vertical effective stresses, respectively. Values chosen are a product of C_cH = 2.75 m, e_0 = 0.5, a depth of 400 m with overlying sediments of density 2000 kg/m^3, and a hydrostatic water column. We estimate the initial effective stress at 400 meters to be 4×10^6 Pa. The change in effective stress since 1992, due to a water table decline of 400 m is 4×10^6 Pa. The vertical displacement due to settlement in one year is then δ_c ~ 2.5 cm. Many combinations of the product of the compaction coefficient and compacting thickness are possible. A compaction coefficient C_c = 0.1 and H = 27.5 m can be interpreted as a 400-meter thick aquifer in which the thickness of clay layers is 27.5 m.

An equivalent specific storage coefficient due to compaction can be calculated from Galloway and Sneed (2013):

(5)$SSk^*=\Delta\bar{b}^*\gamma w\bar{b}0^*\Delta(\sigma zz-\gamma wh)$

where $\Delta\bar{b}=\bar{b}0-\bar{b}$ is the change in thickness of a control volume with initial thickness $\bar{b}0$ of a deformable geologic unit, σ_{zz} is the total vertical stress, *h* the hydraulic head, and γw the specific gravity of water. A change in aquifer thickness relative to its initial thickness of 0.55 m/400 m yields $SSk^*=3.5\times10-6\ m^{-1}$. This value corresponds to a skeletal compressibility of $3.5 \times 10^{-10}\ Pa^{-1}$. Such a value is of the same order of magnitude as the compressibility of water, typical of alluvial sediments (e.g., Hoffmann et al., 2001). Thus, compaction is a plausible mechanism for observed subsidence due to a shallow source, if the water level has indeed declined continuously at Brady since sometime before 2004.

A third possibility is that the reinjected cold water dissolves minerals, as the equilibrium between fluids and reactive minerals is disturbed (e.g., Glassley, 2011, Akin, 2012), and transports them through the producing wells. Mass loss associated with hydrothermal alteration has been suggested as the cause for long-term subsidence at Rotokawa geothermal field in New Zealand (Powell, 2011). At Brady, core samples from well BCH-3 indicate the presence of an argillic alteration zone that extends to a depth of 600 m (Lutz et al., 2011). Assuming a dissolved-solids concentration of 0.25% (the average value for fluids at Brady), rock density of 2500 kg/m^3, and net extraction rate of 200 liter/second, we estimate the rate of mass loss to be ~0.2 liter/second, which is much lower than the rate estimated from modeling of InSAR data. Also, this rate is an upper bound as it requires that all of the solids dissolved in the produced water originate in the same locations as the sources causing the subsidence.

Irrespective of the mechanism of deformation, the InSAR observations indicate a connection between the shallow subsurface and the production wells at Brady. Accordingly, we infer that highly permeable conduits along faults channel fluids to the reservoir tapped by the production wells. In contrast, Desert Peak, a blind geothermal field, located less than 7 km away from Brady, shows little or no deformation in the InSAR dataset, although the two fields are otherwise similar in spatial extent, structural setting, and geothermal production. Desert Peak exhibits neither hydrothermal features nor any evidence of recent surficial fault slip, however, suggesting that the plumbing associated with the fault system there is deeper and more isolated from the surface than at Brady.

Acknowledgments

We thank Hélène Le Mével for helpful discussions. Several figures were created using the Generic Mapping Tools (Wessel and Smith, 1998). We gratefully acknowledge support from the Weeks family to the Department of Geoscience at the University of Wisconsin-Madison. Raw Synthetic Aperture Radar (SAR) data from the ERS, and Envisat satellite missions operated by the European Space Agency (ESA) are copyrighted by ESA and were provided through the WInSAR consortium at the UNAVCO facility. SAR data from the ALOS satellite mission operated by the Japanese Space Agency (JAXA) were acquired from NASA's Distributed Active Archive Center at the Alaska Satellite Facility (ASF). SAR data from the TerraSAR-X and TanDEM-X satellite missions operated by the German Space Agency (DLR) were acquired through Research Project RES1236. This research was supported by grants DE-EE0005510 and DE-EE0006760 from the Geothermal Technologies Office of the U.S. Department of Energy. Elena C. Baluyut was supported by the National Science Foundation Graduate Research Fellowship under grant DGE-1256259.

Appendix A. Supplementary data

The following are the supplementary data to this article:

Download Acrobat PDF file (1MB)Help with pdf files

References

Akin, 2012

S. Akin**Temperature induced dissolution or precipitation in geothermal reservoirs and their effects on pressure transient analysis**

Proceedings of the 37th Workshop on Geothermal Reservoir Engineering, Stanford University, CA (2012)

Ali et al., 2014

S.T. Ali, K.L. Feigl, B. Carr, T. Masterlark, F. Sigmundsson**Geodetic measurements and numerical models of rifting in Northern Iceland for 1993–2008**

Geophys. J. Int., 196 (3) (2014), pp. 1267-1280

CrossRefView Record in Scopus

Ali and Feigl, 2012

S.T. Ali, K.L. Feigl**A new strategy for estimating geophysical parameters from InSAR data: Application to the Krafla central volcano in Iceland**

Geochem. Geophys. Geosyst. (2012), 10.1029/2012GC004112

Allis and Zhan, 2000

R.G. Allis, X. Zhan**Predicting subsidence at Wairakei and Ohaaki geothermal fields, New Zealand**

Geothermics, 29 (4) (2000), pp. 479-497
ArticleDownload PDFView Record in Scopus

Aster et al., 2011

R.C. Aster, B. Borchers, C.H. Thurber**Parameter Estimation and Inverse Problems**
Academic Press (2011)

Baluyut et al., 2015

E. Baluyut, M. Cardiff, K.L. Feigl**Graph theory for analyzing pair-wise data: Applications to interferometric synthetic aperture radar data at Okmok volcano, Alaska**
(2015)
(Unpublished manuscript)

Beauducel et al., 2000

F. Beauducel, P. Briole, J.-L. Froger**Volcano-wide fringes in ERS synthetic aperture radar interferograms of Etna (1992–1998): Deformation or tropospheric effect**
J. Geophys. Res. Solid Earth, 105 (B7) (2000), pp. 16391-16402
CrossRefView Record in Scopus

Benoit and Butler, 1983

W.R. Benoit, R.W. Butler**A review of high-temperature geothermal developments in the northern Basin and Range province**
Geotherm. Resour. Council, 1 (1983), pp. 57-80
View Record in Scopus

Biggs et al., 2007

J. Biggs, T. Wright, Z. Lu, B. Parsons**Multi-interferogram method for measuring interseismic deformation: Denali Fault, Alaska**
Geophys. J. Int., 170 (3) (2007), pp. 1165-1179
CrossRefView Record in Scopus

Bromley et al., 2009

C.J. Bromley, S. Currie, V.R. Manville, M.D. Rosenberg**Recent ground subsidence at Crown Road, Tauhara and its probable causes**
Geothermics, 38 (1) (2009), pp. 181-191
ArticleDownload PDFView Record in Scopus

Carnec and Fabriol, 1999

C. Carnec, H. Fabriol**Monitoring and modeling land subsidence at the Cerro Prieto geothermal field, Baja California, Mexico, using SAR interferometry**
Geophys. Res. Lett., 26 (9) (1999), pp. 1211-1214
CrossRefView Record in Scopus

Chang et al., 2005

H.-C. Chang, L. Ge, C. Rizos**Insar and mathematical modelling for measuring surface deformation due to geothermal water extraction in New Zealand**
International Geoscience and Remote Sensing Symposium, vol. 3 (2005), p. 1587
View Record in Scopus

Chen and Zebker, 2001

C.W. Chen, H.A. Zebker**Two-dimensional phase unwrapping with use of statistical models for cost functions in nonlinear optimization**
J. Opt. Soc. Am. A, 18 (2) (2001), pp. 338-351
CrossRefView Record in Scopus

Coolbaugh et al., 2004

M.F. Coolbaugh, C. Sladek, C. Kratt, G. Edmondo**Digital mapping of structurally controlled geothermal features with GPS units and pocket computers**
Geother. Resour. Counc. Trans., 28 (2004), pp. 321-325
View Record in Scopus

Efron and Tibshirani, 1986

B. Efron, R. Tibshirani**Bootstrap methods for standard errors, confidence intervals, and other measures of statistical accuracy**
Stat. Sci., 1 (1) (1986), pp. 54-75
CrossRefView Record in Scopus

Eneva et al., 2012

M. Eneva, D. Adams, G. Falorni, J. Morgan**Surface deformation in Imperial Valley, CA, from satellite radar interferometry**
Geother. Resour. Counc. Trans., 36 (2012), pp. 1339-1344
View Record in Scopus

Eneva et al., 200

M. Eneva, G. Falorni, D. Adams, J. Allievi, F. Novali**Application of satellite interferometry to the detection of surface deformation in the Salton Sea geothermal field, California**
Geother. Resour. Counc. Trans., 33 (2009), pp. 315-319
View Record in Scopus

Eneva et al., 201

M. Eneva, G. Falorni, W. Teplow, J. Morgan, G. Rhodes, D. Adams**Surface deformation at the San Emidio geothermal field, Nevada, from satellite radar interferometry**
Geother. Resour. Counc. Trans., 35 (2011), pp. 1647-1653
View Record in Scopus

Farr et al., 2007

T.G. Farr, P.A. Rosen, E. Caro, R. Crippen, R. Duren, S. Hensley, M. Kobrick, M.Paller, E. Rodriguez, L. Roth, *et al.***The shuttle radar topography mission**
Rev. Geophys., 45 (2) (2007)

Faulds et al., 201

J.E. Faulds, M.F. Coolbaugh, D. Benoit, G. Oppliger, M. Perkins, I. Moeck, P.Drakos**Structural controls of geothermal activity in the Northern Hot Springs Mountains, Western Nevada: The tale of three geothermal systems (Brady's, Desert Peak, and Desert Queen)**
Geother. Resour. Counc. Trans., 34 (2010), pp. 675-683
View Record in Scopus

Faulds et al., 200

J.E. Faulds, L.J. Garside, R. Chaney**Preliminary geologic map of the Desert Peak-Brady geothermal fields, Churchill County, Nevada**
Nevada Bureau of Mines and Geology (2003)

Feigl et al., 2014

K.L. Feigl, H. Le Mével, S.T. Ali, L. Córdova, N.L. Andersen, C. DeMets, B.S.Singer**Rapid uplift in Laguna del Maule volcanic field of the Andean Southern Volcanic zone (Chile) 2007–2012**
Geophys. J. Int., 196 (2) (2014), pp. 885-901
CrossRef

Feigl and Thurbe

K.L. Feigl, C.H. Thurber**A method for modelling radar interferograms without phase unwrapping: Application to the M 5 Fawnskin, California earthquake of 1992 December 4**
Geophys. J. Int., 176 (2) (2009), pp. 491-504
CrossRefView Record in Scopus

Fialko and Simon

Y. Fialko, M. Simons**Deformation and seismicity in the Coso geothermal area, Inyo County, California: Observations and modeling using satellite radar interferometry**
J. Geophys. Res., 105 (B9) (2000), pp. 21781-21793
CrossRefView Record in Scopus

Foxall and Vasco

B. Foxall, D. Vasco**Inversion of synthetic aperture radar interferograms for sources of production-related subsidence at the Dixie Valley geothermal field.**
Proceedings of the 28th Workshop on Geothermal Reservoir Engineering, Stanford University, CA (2003)

Galloway and Sn

D.L. Galloway, M. Sneed**Analysis and simulation of regional subsidence accompanying groundwater abstraction and compaction of susceptible aquifer systems in the USA**
Bol. Soc. Geol. Mex, 65 (2013), pp. 123-134
CrossRefView Record in Scopus

Gesch et al., 200

D. Gesch, M. Oimoen, S. Greenlee, C. Nelson, M. Steuck, D. Tyler**The national elevation dataset**
Photogram. Eng. Remote Sens., 68 (1) (2002), pp. 5-32
View Record in Scopus

Glassley, 2011

W.E. Glassley**Geothermal Energy: Renewable Energy and the Environment**
CRC Press (2011)

Goldstein and W

R.M. Goldstein, C.L. Werner**Radar interferogram filtering for geophysical applications**
Geophys. Res. Lett., 25 (21) (1998), pp. 4035-4038
CrossRefView Record in Scopus

Hoffmann et al.,

J. Hoffmann, H.A. Zebker, D.L. Galloway, F. Amelung**Seasonal subsidence and rebound in Las Vegas Valley, Nevada, observed by synthetic aperture radar interferometry**
Water Resour. Res., 37 (6) (2001), pp. 1551-1566
CrossRefView Record in Scopus

Hole et al., 2007

J. Hole, C. Bromley, N. Stevens, G. Wadge**Subsidence in the geothermal fields of the Taupo Volcanic Zone, New Zealand from 1996 to 2005 measured by InSAR**
J. Volcanol. Geother. Res., 166 (3) (2007), pp. 125-146
ArticleDownload PDFView Record in Scopus

Igarashi, 2001

T. Igarashi**ALOS mission requirement and sensor specifications**
Adv. Space Res., 28 (1) (2001), pp. 127-131
ArticleDownload PDFView Record in Scopus

Jolie et al., 2012

E. Jolie, J. Faulds, I. Moeck**The development of a 3D structural-geological model as part of the geothermal exploration strategy - a case study from the Brady's geothermal system, Nevada, USA**
Proceedings of the 37th Workshop on Geothermal Reservoir Engineering, Stanford University, CA (2012)

Jonsson, 2009

S. Jonsson**Anthropogenic and natural deformation on Reykjanes Peninsula, southwest Iceland, observed using InSAR time-series analysis 1992–2008**
EGU General Assembly Conference Abstracts, vol. 11 (2009), p. 5142
View Record in Scopus

Krieger et al., 20

G. Krieger, A. Moreira, H. Fiedler, I. Hajnsek, M. Werner, M. Younis, M. Zink**TanDEM-X: A satellite formation for high-resolution SAR interferometry**
IEEE Trans. Geosci. Remote Sens., 45 (11) (2007), pp. 3317-3341
CrossRef

Lutz et al., 2011

S.J. Lutz, A. Zutshi, A. Robertson-Tait, P. Drakos, E. Zemach**Lithologies, hydrothermal alteration, and rock mechanical properties in wells 15-12 and BCH-3, Bradys Hot Springs geothermal field, Nevada**
Geother. Resour. Counc. Trans., 35 (2011), pp. 469-476
View Record in Scopus

Massonnet and F

D. Massonnet, K.L. Feigl**Discrimination of geophysical phenomena in satellite radar interferograms**
Geophys. Res. Lett., 22 (12) (1995), pp. 1537-1540

CrossRefView Record in Scopus

Massonnet and F

D. Massonnet, K.L. Feigl**Radar interferometry and its application to changes in the earth's surface**
Rev. Geophys., 36 (4) (1998), pp. 441-500
CrossRefView Record in Scopus

Massonnet and F

D. Massonnet, T. Rabaute**Radar interferometry: Limits and potential**
IEEE Trans. Geosci. Remote Sens., 31 (2) (1993), pp. 455-464
CrossRefView Record in Scopus

Masters, 2011

E. Masters**Interferometric synthetic aperture radar analysis and elastic modeling of deformation at the Svartsengi geothermal field in Iceland, 1992–2010: Investigating the feasibility of evaluating reservoir pressure changes from low earth orbit (Master's thesis)**
University of Wisconsin, Madison, WI (2011)

McLeod et al., 19

I.H. McLeod, I.G. Cumming, M.S. Seymour**Envisat ASAR data reduction: Impact on SAR interferometry**
IEEE Trans. Geosci. Remote Sens., 36 (2) (1998), pp. 589-602
CrossRefView Record in Scopus

Okada, 1985

Y. Okada**Surface deformation due to shear and tensile faults in a half-space**
Bull. Seismolog. Soc. Am., 75 (4) (1985), pp. 1135-1154
View Record in Scopus

Oppliger et al., 2

G. Oppliger, M. Coolbaugh, W. Foxall**Imaging structure with fluid fluxes at the Bradys geothermal field with satellite interferometric radar (InSAR): New insights into reservoir extent and structural controls**
Geother. Resour. Counc. Trans., 28 (2004), pp. 37-40
View Record in Scopus

Oppliger et al., 2

G. Oppliger, M. Coolbaugh, L. Shevenell**Improved visualization of satellite radar InSAR observed structural controls at producing geothermal fields using modeled horizontal surface displacements**
GRC Trans., 30 (2006), pp. 927-930
View Record in Scopus

Pitz and Miller, 2

W. Pitz, D. Miller**The TerraSAR-X satellite**
IEEE Trans. Geosci. Remote Sens., 48 (2) (2010), pp. 615-622

CrossRefView Record in Scopus

Powell, 2011

T. Powell**Natural subsidence at the Rotokawa Geothermal Field and implications for permeability development**

Proceedings of the New Zealand Geothermal Workshop, Auckland, New Zealand (2011)

Sandwell et al., 2011

D. Sandwell, R. Mellors, X. Tong, M. Wei, P. Wessel**Open radar interferometry software for mapping surface deformation**

EOS Trans. Am. Geophys. Union, 92 (28) (2011), p. 234

CrossRefView Record in Scopus

Sarychikhina et al., 2007

O. Sarychikhina, E. Glowacka, R. Mellors**Preliminary results of a surface deformation study, using differential InSAR technique at the Cerro Prieto geothermal field, BC, México**

Geother. Resour. Counc. Trans., 31 (2007), pp. 581-584

View Record in Scopus

Schmidt and Bürgmann, 2003

D.A. Schmidt, R. Bürgmann**Time-dependent land uplift and subsidence in the Santa Clara valley, California, from a large interferometric synthetic aperture radar data set**

J. Geophys. Res. Solid Earth (1978–2012), 108 (B9) (2003)

Shevenell et al., 2012

L. Shevenell, G. Oppliger, M. Coolbaugh, J. Faulds**Bradys (Nevada) InSAR anomaly evaluated with historical well temperature and pressure data**

Geother. Resour. Counc. Trans., 36 (2012), pp. 1383-1390

View Record in Scopus

Siler and Faulds, 2013

D.L. Siler, J.E. Faulds**Three-dimensional geothermal fairway mapping: Examples from the Western Great Basin, USA**

Geother. Resour. Counc. Trans. (2013), pp. 327-332

View Record in Scopus

Terzaghi and Peck, 1968

K. Terzaghi, R.B. Peck**Soil Mechanics in Engineering Practice**

(2nd ed.), J. Wiley (1968)

Vasco et al., 2013

D. Vasco, J. Rutqvist, A. Ferretti, A. Rucci, F. Bellotti, P. Dobson, C. Oldenburg, J.Garcia, M. Walters, C. Hartline**Monitoring deformation at the Geysers geothermal field, California using C-band and X-band interferometric synthetic aperture radar**

Geophys. Res. Lett. (2013)

Wessel and Smith, 1998

P. Wessel, W.H. Smith**New, improved version of Generic Mapping Tools released**

EOS Trans. Am. Geophys. Union, 79 (47) (1998), p. 579

CrossRefView Record in Scopus

Wicks et al., 2001

C.W. Wicks, W. Thatcher, F.C. Monastero, M.A. Hasting**Steady state deformation of the Coso Range, east central California, inferred from satellite radar interferometry**

J. Geophys. Res., 106 (B7) (2001), pp. 13769-13780

CrossRefView Record in Scopus

Recommended articles

- Geothermal production and reduced seismicity: Correlation and proposed mechanism

Earth and Planetary Science Letters, Volume 482, 2018, pp. 470-477
Download PDFView details

- Using PS-InSAR to detect surface deformation in geothermal areas of West Java in Indonesia

International Journal of Applied Earth Observation and Geoinformation, Volume 64, 2018, pp. 386-396
Download PDFView details

- Geologic remote sensing for geothermal exploration: A review

International Journal of Applied Earth Observation and Geoinformation, Volume 33, 2014, pp. 255-269
Download PDFView details

12Next

Citing articles (12)